Ocean Engineering 363 (2026) 126418

Contents lists available at ScienceDirect

Ocean Engineering

journal homepage: www.elsevier.com/locate/oceaneng

Research paper

Prediction of the performance reduction on the Darrieus vertical-axis tidal-current turbine due to surface roughness when operating in tropical seawater environments

Dendy Satrio [a,*], Soonseok Song [b], Wakana Tsuru [c,**], Mohammad Farid [a], Wimala Lalitya Dhanistha [a], Maktum Muharja [a], Siti Musabikha [d], Herman Pratikno [a]

[a] Institut Teknologi Sepuluh Nopember, Surabaya, 60111, Indonesia
[b] Inha University, Incheon, 22212, South Korea
[c] Institute of Ocean Energy, Saga University, Saga, 840-8502, Japan
[d] National Research and Innovation Agency (BRIN), Banten, 15314, Indonesia

ARTICLE INFO

Keywords:
Ocean renewable energy
Vertical-axis turbine
Marine biofouling
Surface roughness
Computational fluid dynamics
Tropical seawater

ABSTRACT

Darrieus Vertical Axis Turbines (D-VATs) are well suited for Indonesia's low-velocity tidal currents but are highly susceptible to marine biofouling-induced surface roughness under tropical conditions, leading to increased drag and degraded hydrodynamic performance. The impact of surface roughness on D-VAT performance is systematically investigated through full-scale URANS CFD simulations with experimentally derived rough-wall boundary conditions, addressing the roughness scaling limitations commonly associated with model-scale turbine studies. Eight roughness scenarios were evaluated over Tip Speed Ratios (*TSRs*) ranging from 1.2 to 2.8. The results indicate a linear relationship between increasing roughness height and reductions in the power coefficient (C_p). At *TSR* 1.2, C_p decreased by approximately 2% under mild surface roughness conditions (≈0.30 to 0.29) and by up to 39.28% under severe roughness conditions (≈0.30 to 0.18) relative to a smooth surface. Under the most severe roughness condition, the mechanical power (P_{mech}) decreased by up to 62% at *TSR* 2.8 compared to the smooth-surface condition. Increasing *TSR* intensified the performance degradation in both C_p and P_{mech} across all roughness scenarios. Flow contour showed that severe surface roughness promotes widespread turbulent flow and flow separation, weakening pressure loading and torque generation around the turbine blade. The cumulative energy generation further demonstrated that prolonged operation under severe roughness conditions substantially reduces the long-term energy conversion capability of the D-VAT system in tropical marine environments.

Nomenclature:

Abbreviation		
A	Turbine swept area	[m^2]
AR	Aspect ratio	[-]
AEP	Annual Energy Production	[kWh]
BEM	Blade Element Momentum	[-]
C	Chord length	[m]
CFD	Computational Fluid Dynamic	[-]
D	Diameter of turbine	[m]
D-VAT	Darrieus Vertical Axis Turbines	[-]
M	Number of arms	[-]
N	Number of blades	[-]

(*continued on next column*)

(*continued*)

R	Turbine radius	[m]
S	Span length	[m]
S, M, B	Roughness size (Small, Medium, Big)	[-]
SST	Shear Stress Transport	[-]
SMAPE	Symmetric Mean Absolute Percentage Error	[%]
TSR	Tip Speed Ratio	[-]
URANS	Unsteady Reynolds Averaged Navier Stokes	[-]
Symbols		
C_μ	Skin friction coefficient	[-]
C_p	Power coefficient	[-]
$C_{pressure}$	Coefficient of Pressure	[-]

(*continued on next page*)

* Corresponding author.
** Corresponding author.
E-mail addresses: dendy.satrio@its.ac.id (D. Satrio), tsuru@ioes.saga-u.ac.jp (W. Tsuru).

https://doi.org/10.1016/j.oceaneng.2026.126418
Received 9 March 2026; Received in revised form 10 May 2026; Accepted 4 June 2026
Available online 19 June 2026

(*continued*)

C_s	Roughness Constant	[-]
C_t	Torque coefficient	[-]
E	Constant (=9.793)	[-]
Gk	Production of turbulent kinetic energy due to mean velocity gradients	[m^2/s^2]
$G\omega$	Production of specific dissipation rate	[1/s^2]
GCI_{fine21}	Grid Convergence Index for fine grid	[%]
k	Turbulance kinetic energy	[m^2/s^2]
k-ω	Turbulance model	[Kg/m^3]
k^+	Non-dimensional roughness height	[-]
kG	Equivalent sand grain roughness	[m]
k_h	Physical roughness height	[m]
K	Von-Karman constant	[-]
N_1, N_2, N_3	Number of elements for fine, medium, and coarse mesh, respectively	[-]
p	Local static pressure/Apparent order accuracy (depending on context)	[Pa]/[-]
p_∞	Free stream static pressure	[Pa]
P_{mech}	Mechanical power	[W]
$q(p)$	Correction function used in iterative calculation of p	[-]
$r21, r32$	Grid refinement ratio	[-]
r_{ab}	General refinement factor	[-]
s	Sign function, defined as sign(ε_{32} /ε_{21})	[-]
t	Time	[s]
U	Fluid flow velocity	[m/s]
U_p	Near wall velocity	[m/s]
U^*	Wall friction velocity	[m/s]
y^+	First layer thickness	[-]
y_p	Near-wall cell height	[m]
Yk	Dissipation of turbulent kinetic energy	[m^2/s^2]
$Y\omega$	Dissipation of specific dissipation rate	[1/s^2]
ΔB	Roughness shift function	[-]
Γk	Effective diffusivity of turbulent kinetic energy k	[m^2/s]
$\Gamma\omega$	Effective diffusivity of specific dissipation rate ω	[m^2/s]
ε_{21}	Difference between fine and medium solutions, $\phi_1 - \phi_2$	[-]
ε_{32}	Difference between medium and coarse solutions, $\phi_2 - \phi_3$	[-]
τ_w	wall shear stress	[Pa]
μ	Fluid dynamic viscosity	[Pa.s]
ρ	Fluid density	[kg/m^3]
ω	Angular velocity/specific dissipation rate (depending on context)	[rad/s]/[1/s]
φ	Preset angle	[rad]
σ	Turbine solidity	[-]
∇	Gradient operator	[-]
ϕ	Solution variable (output parameter)	[-]
ϕ_1, ϕ_2, ϕ_3	Solution values for fine, medium, and coarse meshes	[-]
$\phi ext21$	Extrapolated value based on fine and medium grids	[-]
$ea21$	Approximate relative error between fine and medium grids	[-]
$eext21$	Extrapolated relative error	[-]

1. Introduction

With 17,024 islands, Indonesia is known as an archipelagic country. It should come as no surprise that Indonesia has numerous, narrow straits connecting its islands. The islands also enclose Indonesia's sea and create a shorter fetch distance. These two factors contribute to Indonesia's relatively low ocean current velocity (Madi et al., 2024; Satrio et al., 2026). However, straits like the Larantuka Strait have current velocities over 3 m/s, far higher than those in the open sea (Firdaus et al., 2017). As a result, some of the narrow strait was identified as a possible site for developing an ocean current energy converter (Erwandi et al., 2024; Firdaus et al., 2017; Satrio et al., 2025).

Hydrokinetic turbines encompass a wide range of configurations, particularly vertical axis water turbines (VAWTs), which can be classified into lift-based and drag-based rotors. Lift-based turbines, such as Darrieus and Gorlov rotors, generate torque primarily through lift forces and generally offer higher C_p around 0.3 – 0.4 (Akhlagi et al., 2023; Etemadeasl et al., 2025). In contrast, drag-based turbines such as Savonius rely on drag forces and typically exhibit lower efficiency but better self-starting characteristics (Ghafoorian et al., 2024). The Gorlov rotor, often considered a helical VAWT, has been widely applied in low-head and low-velocity hydraulic conditions. Previous studies on Gorlov and Savonius turbines highlight the distinct characteristics of each configuration. Among these, the D-VATs offers a favorable balance of efficiency and performance, making it the focus of this study.

Based on its location on the equator, Indonesia receives consistent exposure to sunlight every year, making it a country with tropical climate. This condition has a direct impact on Indonesia's sea surface temperature, which has been measured in research by Kusuma et al. (2017) from 2007 to 2016, ranging from 28°C to 31°C. Another study by Ffield and Robertson (2008) also recorded a decrease in Indonesian sea temperature of 0.067°C per meter. This data indicates that within certain depths, where ocean current energy converters can be applied, temperatures remain relatively warm.

New challenges arise in efforts to implement marine energy converters, warm tropical waters tend to be an ideal environment for marine biofouling organisms to develop more quickly (Darvehei et al., 2018), and according to Hadiyanto (2018), the species richness of marine biofouling organisms found in Indonesia's water is higher than in other tropical regions. Fig. 1 (a) shows the marine biofouling cleaning process of the kobold turbine from INSEAN's Enermar pilot plant. Less severe fouling was also encountered in the Cobscook Bay Tidal Energy Project of the Ocean Renewable Power Company (ORPC) in Maine, as presented in Fig. 1 (b). As another example (Starzmann et al., 2022) reported observations on an ocean turbine operating under real sea conditions for approximately four years, resulting in an estimated roughness height of 2–10 mm at 75% blade span.

All the problems above are increasingly becoming serious, where in Fig. 2 Uzun et al. (2019), which summarizes the growth of calcareous-type marine biofouling organisms (barnacles, mussels, tubeworms, etc.): between equatorial waters which are in fact tropical waters, and Mediterranean waters which are in fact subtropical waters. The graph below shows that in tropical waters shown in the equatorial region, marine biofouling growth reached a value of 100 fouling rating on the 379th day, while in Mediterranean waters, the value of 100 fouling rate was only reached on the 726th day.

Previous experimental research about the effect of surface roughness on horizontal axis tidal turbine systems had been carried out, although only in a limited number of literature. Walker et al. (2020) investigated the effect of macroorganism biofouling on the performance of the AHH19 tidal turbine section type using a wind tunnel. The turbine section is fitted with the barnacle model of 11 mm height (0.02C). They found that the barnacle only has a limited effect on lift performance, while drastically increasing drag up to 75%, with 50% of the blade effected with barnacles.

Starzmann et al. (2022) also employed experimental testing and Blade Element Momentum (BEM) simulation to analyze the effect of marine biofouling on the performance of the SIT 250 horizontal axis turbine. Three fouling conditions were compared: clean, fouled, and clean pressure sides of the turbine. The macroorganism is primarily algae with roughness height ranging from 2 to 10 mm (0.006 – 0.03C). The results show that the turbine with fouled condition performs the worst, with up to 47% power drop and 28% thrust reduction. Some research about the surface roughness effect on horizontal axis turbines was performed using numerical simulation.

Song et al. (2020) studied the turbine performance for ten marine biofouling variations from Demirel et al. (2017). The study utilized the modified wall function approach with the k-ω shear stress transport (SST) turbulence model to capture the turbine surface roughness. They establish that the increase in surface roughness directly correlates to the reduction in the turbine's C_p. The C_p reduction ranges from 13% at the designed TSR to 215% at TSR = 8. They also found that the surface roughness can reduce the optimum TSR point where the highest C_p is found, resulting in a narrower operational window for the turbine. Farkas et al. (2022) conduct similar numerical simulations to Song et al. (2020) with six different fouling conditions. A similar trend is also found with a C_p decrease equal to 10.70% at optimum TSR and 31.44% at

(a) (b)

Fig. 1. Marine biofouling found at the surface of (a) Kobold turbine (Moroso, 2007) and (b) Tidal Current Turbine (Song et al., 2020).

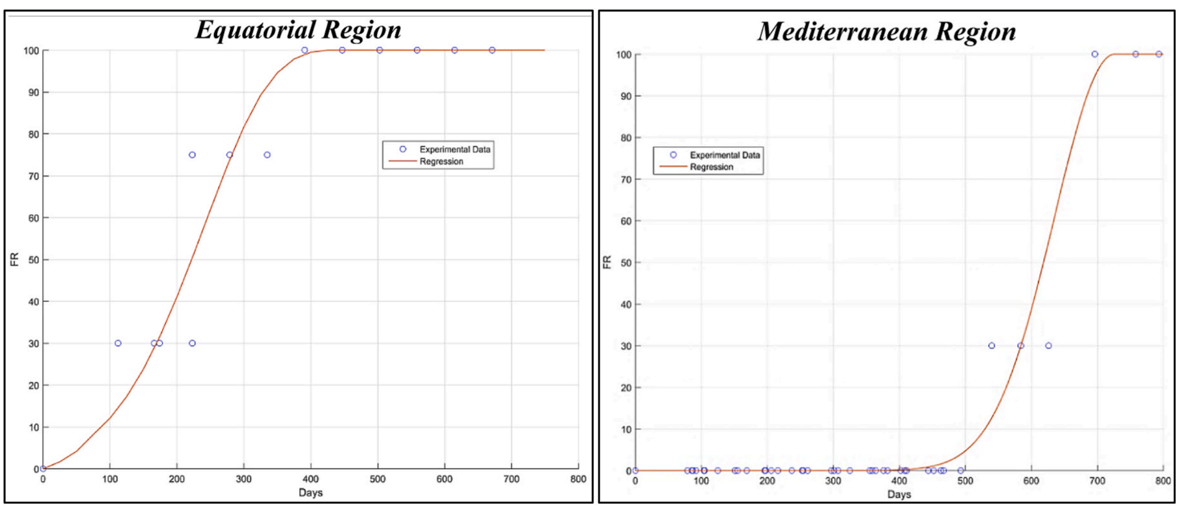

Fig. 2. Comparison of marine biofouling growth between equatorial waters and mediterranean waters (Uzun et al., 2019).

$TSR = 10$.

D-VAT performance reduction due to surface roughness has also been investigated. Priegue and Stoesser (2017) carry out experimental research to study the effect of surface roughness, turbine solidity, and number of blades against the performance of D-VAT. The result indicates that the rough surface can negatively affect the turbine performance, regardless of the other parameters. It is proven that the performance penalty becomes more significant with a rougher surface and a higher Reynolds Number. Khanjanpour and Javadi (2020) performed both experiments and numerical studies to examine the effect of blade roughness on D-VAT performance. Both models (experiment and numeric) have the exact dimensions, setup, and five roughness height variations. It is concluded that blade roughness can reduce the maximum power output with values of 27% and 22% for numerical and experimental methods, respectively.

Previous studies have demonstrated that marine biofouling and surface roughness can significantly degrade turbine performance through increased drag and altered operating characteristics. While both experimental and numerical approaches have successfully captured these effects, most existing studies focus on model-scale configurations or horizontal-axis turbines. As a result, the *TSR*-dependent influence of roughness severity on full-scale Darrieus vertical axis turbines remains insufficiently understood, motivating the present investigation.

Despite growing experimental and numerical efforts to investigate surface roughness effects on tidal turbines, a systematic full-scale assessment of roughness-induced performance degradation in D-VAT operating under low-velocity tidal currents remains insufficiently understood, particularly under full-scale operating conditions. Most existing studies are conducted at model scale, whereas the direct transfer of roughness parameters across scales is known to be non-trivial and may lead to unrepresentative hydrodynamic behavior.

While preserving physically representative roughness behavior at full scale, the present study conducts a full-scale CFD investigation on a D-VAT configuration scaled to the dimensions of the Insean Enermar (Kobold) tidal turbine, quantifying the influence of surface roughness across eight distinct roughness scenarios over a broad range of *TSRs*. The overall logical framework of the present numerical investigation is summarized in Fig. 3.

2. Material and methods

2.1. Turbulence model

The CFD model for this study employs the URANS method with k-ω Shear Stress Transport (SST) as the turbulence closure. All the previous numerical simulations about turbine surface roughness, e.g., (Farkas et al., 2022; Khanjanpour and Javadi, 2020; Song et al., 2020), also utilize the k-ω turbulence model. It is based on the Wilcox k-ω equations

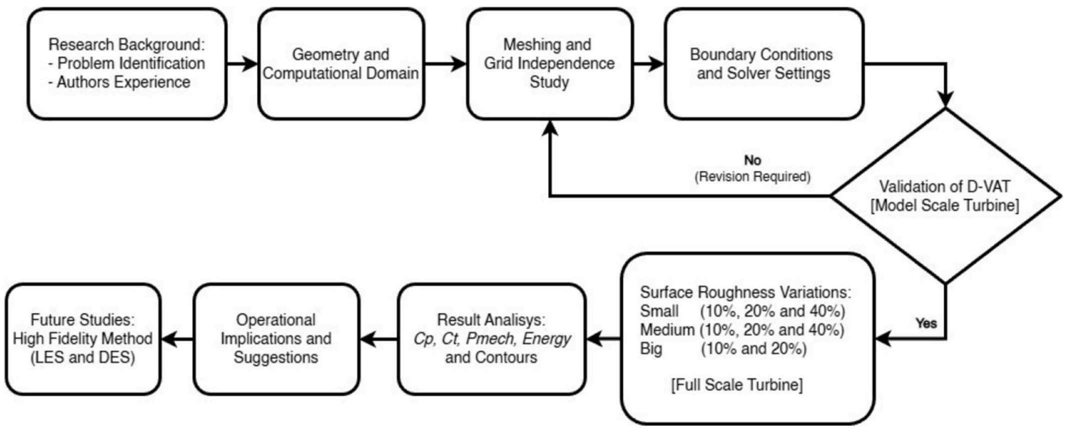

Fig. 3. Logical framework of the present CFD investigation on roughness effects in D-VATs.

(Robinson and Hassan, 1996) with modifications to account for the shear stress transport equations. The two equations of the transport equation for the Fluent CFD code can be written as:

$$\frac{\partial(\rho k)}{\partial t} + \nabla.(\rho U k) = \nabla.(\Gamma_k \nabla k) + G_k - Y_k \tag{1}$$

and

$$\frac{\partial(\rho \omega)}{\partial t} + \nabla.(\rho U \omega) = \nabla.(\Gamma_\omega \nabla \omega) + G_\omega - Y_\omega \tag{2}$$

Where U: mean velocity; ρ : fluid density; k: turbulence kinetic energy; ω : specific dissipation rate; Γ_k and Γ_ω: he effective diffusivity of k and ω, respectively; G_k and G_ω: the generation of k and ω due to mean velocity (convection term); Y_k and Y_ω: the dissipation of k and ω due to turbulence.

The k-ω SST formulation includes some refinements to eliminate the sensitivity to the freestream values of k and ω found in the conventional k-ω turbulence model. It utilizes a blending function to transform from the k-ω model at near wall boundary conditions into the k-ε model at freestream flow (ANSYS Inc, 2020). The blending function directly correlates to the normal wall distance, which highlights the importance of the $y+$ value of the near wall mesh. The recommended $y+$ value of the first layer height is one, as demonstrated (Khanjanpour and Javadi, 2020).

2.2. Roughness function

The presence of surface roughness modifies the velocity profile in the near-wall region compared to a smooth surface. In this study, surface roughness is implemented using a rough-wall-function approach, where roughness effects are applied as boundary condition parameters rather than being resolved geometrically in the mesh (ANSYS Inc, 2020).

Specifically, the roughness is represented using a virtual roughness treatment through the equivalent sand-grain roughness concept, where the roughness effect is incorporated by modifying the near-wall velocity profile instead of physically resolving the surface geometry within the mesh. In this approach, the roughness parameters act directly on the wall function formulation to account for the influence of surface irregularities on wall shear stress and near-wall turbulence behavior. This method enables the hydrodynamic effects of marine biofouling roughness to be captured in a numerically stable and computationally efficient manner while avoiding excessive mesh refinement requirements near the wall region (ANSYS Inc, 2020; Grigson, 1992).

As a result, the roughness does not physically extend into or overlap the first grid cell, since the effective wall location is virtually shifted to ensure numerical stability (Hasfanizam et al., 2024; Yassin et al., 2021). With this, the velocity profile near the wall in the presence of surface roughness can be described using a modified wall roughness law (Pattanapol et al., 2008), with the following equation:

$$\frac{U_p U^*}{\tau_w/\rho} = \frac{1}{K}\ln\left(E\frac{\rho U^* y_p}{\mu}\right) - \Delta B \tag{3}$$

where U_p: near-wall velocity at cell center p; τ_w: wall shear stress; K: Von-Karman constant; E: is constant (=9.793); y_p: near-wall cell height; μ: fluid dynamic viscosity; and U^*: the wall friction velocity which can be written as:

$$U^* = C_\mu^{1/4} k^{1/2} \tag{4}$$

where C_μ: skin friction coefficient.

The value of ΔB is different between three distinct regimes: hydrodynamically smooth ($k^+ \le 2.25$), transitional ($2.25 < k^+ \le 90$), and fully rough ($k^+ > 90$). The non-dimensional roughness height (k^+) is equal to $\frac{\rho k_h U^*}{\mu}$, where k_h is the physical roughness height. The fluent CFD code adopts the formula from (Tuncer and Peter, 1984) to calculate the ΔB. The roughness effect is negligible in the smooth regime, resulting in $\Delta B = 0$. While the translational regime uses the formula below:

$$\Delta B = \frac{1}{K}\ln\left[k^+ - \frac{2.25}{87.75} + C_s k^+\right] \times \sin\{0.4528(\ln k^+ - 0.811)\} \tag{5}$$

Lastly, the formula for fully rough regime is:

$$\Delta B = \frac{1}{K}\ln(1 + C_s k^+) \tag{6}$$

where C_s: roughness constant (Zhao et al., 2013).

The fluent CFD code needs the values of k_h and C_s in order to model the roughness effect. The fluent User Guide recommends the use of equivalent sand grain roughness as the value of k_h. There is no clear guideline to choose the correct value of C_s that represents the uniformity of the roughness height, However, in the configuration of three regimes as used in ANSYS, typically in several references, the values of Cs are 0.253, 0.26 (Tuncer and Peter, 1984; Demirel et al., 2017), and 0.5, is the setting that is used as the default by Ansys CFD in its calculations (ANSYS Inc, 2020). Meanwhile, the configuration of roughness in this study refers to Song et al. (2020), where the results he obtained refer to the results previously stated by Grigson (1992) with a single regime configuration and using a value of $Cs = 1$, then to accommodate the differences in the equations used, the value of $Cs = 1$ is used, and the equation can be rewritten as below.

$$\Delta B = \frac{1}{K}\ln(1 + k^+) \tag{7}$$

To prevent singularity issues for large values of k_h, Fluent virtually shifts the cell's first layer height by 50% of the roughness height.

2.3. Geometry of the vertical-axis turbine

The vertical axis turbine model of the present work is based on previous research by (Zhao et al., 2013). The exact dimensions of Zhao's turbine are presented in Table 1, However, the roughness dimenssion could not be directly applied to the model-scale turbine due to unproportional scaling, as stated by Song et al. (2020). Therefore, it is essential to scale the Zhao's turbine to the size of the kobold turbine from Insean's Enermar pilot plant. The scaled dimensions are also presented in Table 1 as "Full-Scale", which will be modeled and analyzed further in this study. The visual representation of the turbine geometry parameters can be seen in Fig. 4.

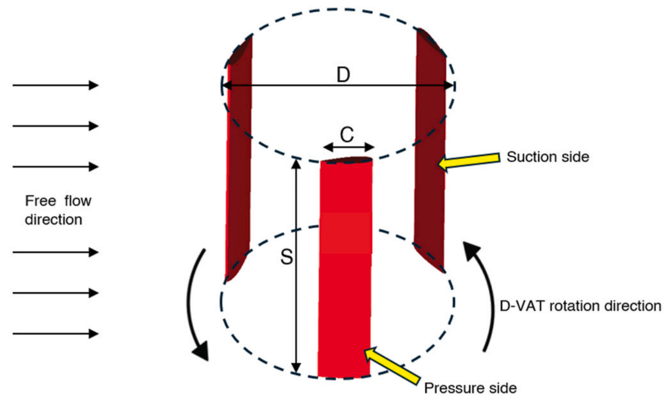

Fig. 4. Geometry parameters in the D-VAT.

2.4. Computational domain and boundary conditions

The present study employs 3D simulation for the validation and grid independence studies. The simulation is done in transient conditions to portray the turbine rotation. As such, the computational domain is sliced into two smaller domains, which are stationary and rotary domains, as shown in Fig. 5. Both the model and full-scale domain have exactly the same non-dimensional size as explained below.

The fluid region is represented by the stationary domain, while the rotating turbine is depicted by the rotary domain. The rectangular stationary domain has dimensions of 10D in width, 15D in length, and 5S in height, selected to minimize blockage effects on turbine performance Mannion et al. (2018) and to ensure sufficient flow development (Rezaeiha et al., 2018). In particular, the computational domain extends 5D upstream from the turbine center toward the inlet and 10D downstream toward the outlet, following domain configurations commonly adopted in prior studies (Satrio et al., 2024).

It is noted that computational studies involving air as the working fluid often employ larger computational domains, as aerodynamic flows typically exhibit slower wake recovery (Ghafoorian et al., 2024; Porté-agel et al., 2020). In contrast, hydrodynamic flows in water, due to higher fluid density and stronger turbulent momentum, generally exhibit faster wake recovery, with previous studies reporting flow re-stabilization within approximately 8D downstream (Ouro and Stoesser, 2019). Accordingly, the adopted domain size is sufficient to capture wake development and recovery in the present water-based simulations and is consistent with domain configurations commonly used in prior CFD studies of marine turbines (Satrio et al., 2024).

The type of boundary conditions utilized is depicted in Fig. 5. A constant velocity inlet of 0.25 m/s and 1.5 m/s is applied for the model- and full-scale cases, respectively, while the outlet is defined as a pressure outlet. The inlet velocities and corresponding rotational speeds are prescribed to maintain an identical *TSR* between the model-scale and full-scale simulations. By enforcing *TSR* similarity, the advance angle, blade angle of attack, and pressure distribution along the turbine blades remain consistent across scales, resulting in comparable turbine loading conditions (Shi et al., 2013).

The side boundaries are treated as symmetry planes to prevent interference with the freestream flow by enforcing zero normal velocity and zero normal gradients. The turbine blade is defined as a smooth wall during validation and later assigned as a rough wall based on the surface roughness variations presented in Table 4.

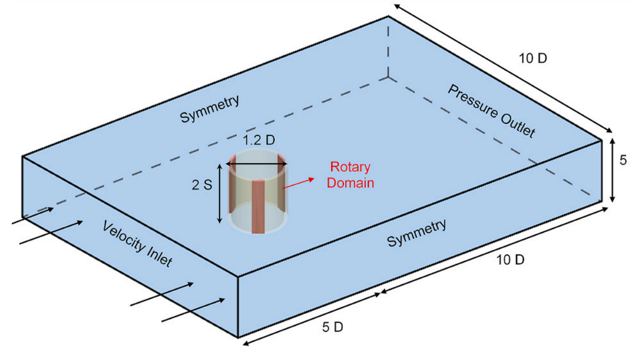

Fig. 5. Computational domain and boundary conditions setup.

To accurately capture the unsteady flow characteristics around the blade surface while maintaining computational efficiency, the simulation employs a URANS approach with the k-ω SST turbulence model. Although higher-fidelity methods such as Large Eddy Simulation (LES) and Detached Eddy Simulation (DES) can provide detailed flow resolution, they require significantly higher computational resources (Alkhabbaz et al., 2024; Daabo et al., 2024). In contrast, the k-ω SST model offers a reliable balance between accuracy and computational cost, with proven capability in handling wall-bounded flows and adverse pressure gradients (Utama et al., 2020). A summary of the applied boundary conditions and solver configuration is provided in Tables 2 and 5.

Table 1
Turbine geometry design parameters.

Parameters	Model Scale	Full Scale
Foil type	NACA 0018	NACA 0018
Chord length (C)	0.12 m	0.72 m
Diameter of turbine (D)	1 m	6 m
Span length (S)	0.66 m	3.96 m
Number of blades (N)	3	3
Number of arms (M)	6	6
Preset angle (φ)	0°	0°
Solidity ($\sigma = N.C/D$)	0.36	0.36
Aspect ratio (AR=S/D)	0.66	0.66

Table 2
Boundary conditions applied in the CFD simulations.

Boundary	Specification
Inlet	Uniform velocity (model scale: 0.25 m/s; full scale: 1.5 m/s)
Outlet	Pressure outlet
Side boundaries	Symmetry
Turbine blade	Smooth wall (validation); rough wall (parametric study)
Rotary interface	Sliding mesh
Fluid	Seawater ($\rho = 1025$ kg/m^3)
Stationary domain	(width × length × height) (10D × 15D × 5S)
Upstream distance	5D
Downstream distance	10D
Rotary domain D	1.2 D blade
Rotary domin height	2S

Table 3
Summary of the mesh quality and quantity parameters.

Parameter	Coarse	Medium	Fine
Node count	912,223	2,288,775	2,556,001
Element count	1,946,999	3,379,260	6,207,658
Average skewness	0.36	0.21	0.31
Average orthogonal quality	0.67	0.81	0.71
Average aspect ratio	92.2	39.2	43.6
Inflation number	20	20	20
Inflation growth rate	1.2	1.2	1.2
Nodes around blade	100	240	320

Table 4
Surface roughness variations.

	Variations	k_G (μm)	k_h (mm)	Surface coverage (%)
	S10%	24	1.25	10
	S20%	63	1.25	20
	S40%	149	1.25	40
	M10%	84	2.5	10
	M20%	165	2.5	20
	M40%	388	2.5	40
	B10%	174	5	10
Area of application	B20%	489	5	20

Table 5
Solver setup applied in the CFD simulations.

Solver Set-up	Specification
Simulation type	3D, transient
Turbulence model	URANS, k–ω SST
Temporal discretization	Second-order implicit
Spatial discretization	Second-order
Pressure–velocity coupling	COUPLED
Residual convergence criterion	10^{-6} (continuity, momentum, turbulence)
Time formulation	Transient

2.5. Meshing generation

To ensure accuracy, a grid independence investigation is conducted by adjusting the element size along the edges and body of the model geometry. Table 3 provides the exact number of mesh elements for each of the three mesh layouts. The element size is progressively reduced from the coarse mesh while maintaining consistent meshing methods and prism layer settings. Fig. 6 illustrates the instantaneous torque generated by the D-VAT at a *TSR* of 1.75. The results indicate that the torque values for the medium mesh (yellow line), fine mesh (green line), and coarse mesh (red line) are closely aligned. Considering the balance between computational accuracy and time constraints, the medium mesh option is selected for subsequent studies.

Assessing the produced mesh quality is equally crucial as determining the mesh element count. Table 3 presents mesh quality metrics for the three different mesh configurations. With the exception of the coarse mesh's aspect ratio, all parameters indicate that acceptable quality meshes have been constructed (ANSYS Inc, 2020). It is also important to note that the medium mesh option provides the highest-quality mesh. This might be because the medium mesh setting provided the smoothest transition from the prism layer to the volume mesh.

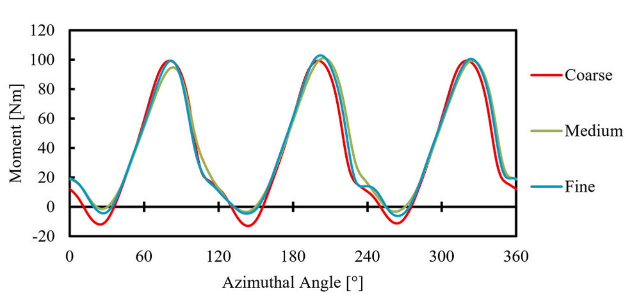

Fig. 6. Grid independence study of the generated D-VAT moment in *TSR* 1.75 for the 3 different mesh configurations.

Fig. 7 depicts the mesh configuration used in this study. Fig. 7 (a) shows the section plane of the computational domain at the middle of the domain height. More than 99% of the total mesh element is distributed in the rotary domain. The interface between the stationary and rotary domains is non-conformal, with the exact element sizing. The detailed mesh configuration on the rotary domain is conveyed in Fig. 7 (b). The rotary domain comprises five individual bodies with conformal interfaces in between. The near-wall treatment of the turbine blade mesh is illustrated in Fig. 7 (c). Prism layer meshes are employed to refine the near-wall region, with the first-layer cell thickness selected such that the y^+ values remain higher than 30 and k^+, in accordance with recommendations from Demirel et al. and CD-adapco.

2.6. Surface roughness variations

The surface roughness variations in this study were derived from experimental data by Demirel et al. (2017) and Song et al. (2020) where the maximum roughness height was 1.25 and the surface coverage was limited to 50%. As shown in Table 4, the selected coverage ratios (10%, 20%, and 40%, with B-type limited to 20%) are based on empirical evidence indicating that frictional drag effects tend to reach a saturation plateau at approximately 40–50% surface coverage (Demirel et al., 2017). Beyond this range, further increases in coverage yield marginal hydrodynamic differences, while variations in roughness size were found to exert a more dominant influence than coverage alone. Beyond this range, further increases in coverage result in only marginal hydrodynamic changes, whereas variations in roughness size exhibit a more pronounced effect.

The equivalent sand grain roughness (*kG*) was calculated based on barnacle fouling's roughness height and surface coverage, serving as an input parameter for the CFD simulation's wall boundary conditions. Eight roughness variations were analyzed, each named using a combination of an alphabet to indicate barnacle size "S," "M," and "B" for small, medium, and big barnacles, respectively and a percentage to denote surface coverage. This naming scheme follows the conventions established in prior studies.

2.7. Solver setting and performance parameter

The sliding-mesh approach is implemented in transient conditions to run the simulation. This is done to allow the rotary domain to spin for each *TSR* at a consistent rotating velocity. It is calculated that the turbine in this investigation has a Reynolds Number of 2.1 x 10^6. The *k-ω* SST turbulence model can produce an accurate prediction of flow separation over a smooth surface (ANSYS Inc, 2020). A maximum of 10 iterations is allowed for each time step, with the time step size set to 2° of turbine rotation. Some performance parameters that is essential when comparing turbine efficiency are presented below:

$$TSR = \frac{\omega R}{U} \tag{8}$$

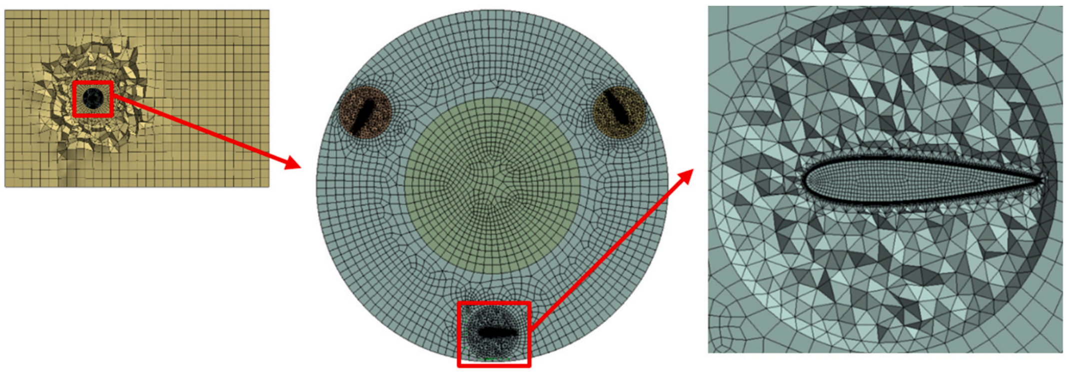

Fig. 7. Preview of the mesh configuration in (a) stationary domain, (b) rotary domain, and (c) surface of D-VAT.

$$Cm = \frac{Moment}{0.5\,\rho\,A\,R\,U^2} \tag{9}$$

$$Cp = \frac{Power}{0.5\,\rho\,A\;U^3} \tag{10}$$

$$\%\ \Delta Cp = \frac{(Cp_1 - Cp_2)}{Cp_1} \times 100\% \tag{11}$$

$$C_{pressure} = \frac{(p - p_\infty)}{\frac{1}{2}\rho U^2} \tag{12}$$

$$U_\tau = \frac{\sqrt{\frac{\tau_{wall}}{\rho}}}{\frac{1}{2}\rho U^2} \tag{13}$$

where ρ: fluid density (kg/m^3); U: free stream velocity (m/s); A: turbine swept area (m^2); R: turbine radius; ω: turbine rotational velocity (rad/s); p: local static pressure (Pa); p_∞: free stream static pressure (Pa); and τ_{wall}: wall shear stress (Pa).

The ratio of rotational velocity to free-stream velocity is commonly referred to as the *TSR*. The resulting moment of the simulation can be used to determine the coefficient of moment (C_m). The final equation gives the C_p, which is usually used to verify numerical results and assess the relative performance of the turbine. The relative percentage of C_p can be calculated by deducting the smooth surface model C_{p1} with rough wall model C_{p2}, divided by C_{p1} times a hundred percent.

There are also 2 important equations used in the contour analysis section below. The first one being the coefficient of pressure ($C_{pressure}$), which is a non-dimensional parameter that can be used to compare pressure distribution across an object's surface. The second is the non-dimensional shear stress (non-dimensional U_τ), calculated by dividing the wall shear stress with the dynamic pressure.

3. Results and discussion

3.1. Verification study

To assess the numerical errors of the CFD model and choose an appropriate mesh sizing, a verification study was carried out. The order of accuracy of the simulation model was estimated using the Grid Convergence Index (GCI) method, which is based on Richardson's extrapolation method (Richardson, 1910). A recent study by Celik et al. (2008) implemented the Richardson extrapolation to estimate the uncertainty of CFD applications, which calculates the apparent order p by using the following formula:

$$p = \frac{1}{\ln(r_{21})}\left|\ln\left|\frac{\varepsilon_{32}}{\varepsilon_{21}}\right| + q(p_a)\right| \tag{14}$$

$$q(p) = \ln\left(\frac{r_{21}^p - s}{r_{32}^p - s}\right) \tag{15}$$

$$s = 1 \cdot sign\left(\frac{\varepsilon_{32}}{\varepsilon_{21}}\right) \tag{16}$$

with r_{ab} (refinement factor) $= \sqrt[3]{N_b/N_a}$ for a 3D simulation. N represents the number of elements for a given configuration. While $\varepsilon_{ab} = \phi_a - \phi_b$, with ϕ represents the output parameters, which were C_m and C_p. It is important to note that fixed-point iteration can solve equations, with the starting value of q(p) equals zero.

The extrapolated values then can be calculated from:

$$\phi_{ext}^{21} = \left(\frac{r_{21}^p \phi_1 - \phi_2}{r_{21}^p - 1}\right) \tag{17}$$

Moreover, the approximate and extrapolated relative error can be calculated using:

$$e_a^{21} = \left|\frac{\phi_1 - \phi_2}{\phi_1}\right| \tag{18}$$

$$e_{ext}^{21} = \left|\frac{\phi_{ext}^{21} - \phi_1}{\phi_{ext}^{21}}\right| \tag{19}$$

Finally, to obtain the fine-grid convergence index, the below formulation can be employed:

$$GCI_{fine}^{21} = \frac{1.25 e_a^{21}}{r_{21}^p - 1} \tag{20}$$

In this study, three different mesh configurations were utilized: coarse (N_3), medium (N_2), and fine (N_1) mesh. Table 6 presents the calculated parameters for GCI using the formula described before. The values of C_p and C_t were obtained at $TSR = 1.75$ for the baseline turbine model. It can be seen that the numerical uncertainties for C_p and C_t using the medium mesh are 1.22%. The value is quite different from Song et al. (2020), which achieved a C_p of 0.24% and a C_t of 0.04%. However, things could happen where Song et al. (2020) use a fine mesh configuration while author use a medium mesh configuration. Even so, the values attained here have not yet reached 2%. Therefore, the author assumes these values can be tolerated.

3.2. Numerical validation of the baseline turbine

In the validation process, parameters from Zhao et al. (2013) should be used. However, to meet real-world performance expectations, the turbine in model scale needs to be adjusted to actual size because the roughness size and the resulting effects cannot provide accurate results if

Table 6
Discretization error calculation for spatial convergence study.

	C_p	C_t
N_1	6207658	6207658
N_2	4802129	4802129
N_3	3379260	3379260
r_{21}	1.09	1.09
r_{32}	1.12	1.12
Φ_1	0.18632	0.106469
Φ_2	0.191044	0.109168
Φ_3	0.172256	0.098432
ε_{32}	−0.01879	−0.01074
ε_{21}	0.004724	0.002699
s	−1	−1
e_a^{21}	−0.02535	−0.02535
q	−0.386	−0.386
p	14.94045	14.94045
ϕ_{ext}^{21}	0.184497	0.184497
e_{ext}^{21}	0.99%	0.99%
GCI_{medium}^{21}	1.22%	1.22%

it remains at the model scale. This rescaling is done with a ratio of 1:6, inspired by several parameter sizes of the Kobold turbine from INSEAN's Enermar pilot plant (Moroso, 2007), as shown in Table 1.

Fig. 8 compares the obtained C_p from the present 3D numerical simulations and the experimental data of Zhao et al. (2013). The numerical simulations successfully replicate the general trend of the experimental data. Initially, during the first phase, a consistent trend in values was observed. Specifically, the C_p values from the numerical study, starting at *TSR* 1.2, steadily increased in line with experimental C_p values. Although there was a slight discrepancy at the peak achievement, *TSR* 2.29, where the experimental C_p reached 0.29 while the numerical simulation C_p hovered close at 0.26, this deviation was temporary. Subsequently, post-peak phase, the values exhibited conformity once more, declining consistently until *TSR* 2.8. Furthermore, the alignment was quantified using the Symmetric Mean Absolute Percentage Error (sMAPE) approach, as described by equation (21).

$$SMAPE = \frac{100}{n} \sum_{j}^{n} \frac{2 \times |e_j|}{|A_j| + |P_j|} \tag{21}$$

Here, (n) represents the number of data points, while (e_j) denotes the error for data point j, calculated as the difference between the Experiment's C_p value (A_j) and the numerical simulation's C_p value (P_j) (Tayman and Swanson, 1999). This calculation indicates that the numerical simulation results are highly accurate, with an error of just 0.6%. Thus, the study using this numerical modeling approach can be deemed valid.

3.3. Numerical simulation results of modified blade surfaces variations

As shown in Fig. 9, the reduction in C_p increases with both larger barnacle size and higher surface coverage. It can be observed that the "M40%" variation performs much worse than the "B10%" variation, and only slightly better than the "B20%" variation. Similarly, the "S40%" variation performs worse than the "B10%" variation. Therefore, the effect of surface roughness is always influenced by these two factors, both of which play an equally important role and should be considered.

Song et al. (2020) found that surface roughness can lower the *TSR* where the maximum C_p is obtained, therefore reducing the operational window of the horizontal axis tidal turbine. The present study also observes the same behaviour, although the optimum *TSR* is higher compared to the baseline turbine. To further explain the mechanism behind this performance degradation, the variation of the instantaneous turbine coefficient of moment (C_m) during blade rotation is also evaluated.

The turbine C_m curve further clarifies the mechanism behind the performance degradation observed in Fig. 10. Since the turbine C_p is directly influenced by the torque generated during blade rotation, the reduction in C_m under increasing roughness conditions explains the progressive decrease in turbine performance. As shown in Fig. 10, the Smooth configuration produces the highest maximum C_m value of approximately 0.368 at a rotation angle of 586°, which is higher than those of S20% (0.353), M20% (0.348), and B20% (0.283). Within the rotation angle range of 572°– 600°, the Smooth configuration consistently maintains higher C_m values, reflecting its capability to generate biggest torque during the primary torque-producing phase.

In addition, the Smooth configuration exhibits a more gradual reduction in C_m after reaching its peak value, suggesting a more stable pressure distribution and tangential force generation along the blade surface. In contrast, increasing roughness severity progressively reduces the moment amplitude, with the B20% condition showing the most significant weakening of the torque response. This behavior indicates that surface roughness weakens the blade's ability to maintain favorable flow attachment and effective pressure differences during rotation, thereby directly contributing to the reduction in turbine C_p observed in the previous analysis.

Table 7 summarizes the percentage change in the *TSR* at which the maximum C_p occurs for all surface roughness variations. The smooth-surface condition is used as the baseline reference, against which the C_p performance of each roughness configuration is compared. The parameter Δ (%) represents the relative difference between the baseline and each roughness case, expressed as a percentage, thereby highlighting the shift in optimal operating *TSR* induced by surface roughness.

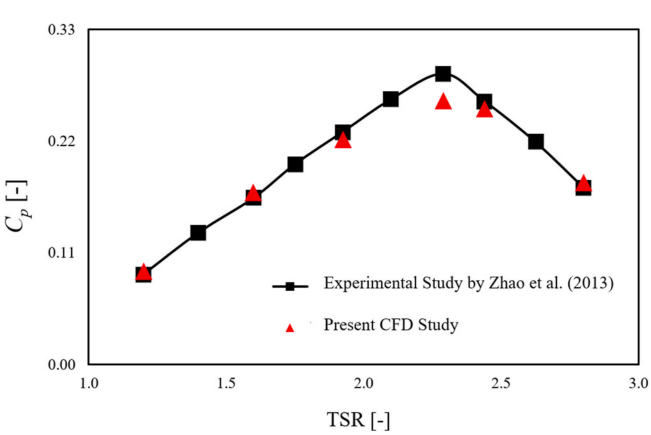

Fig. 8. C_p validations against the experimental data of Zhao et al. (2013).

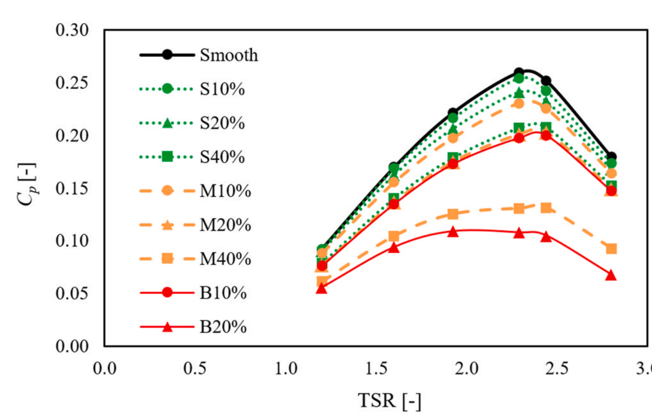

Fig. 9. C_p reduction for all variations of the surface roughness.

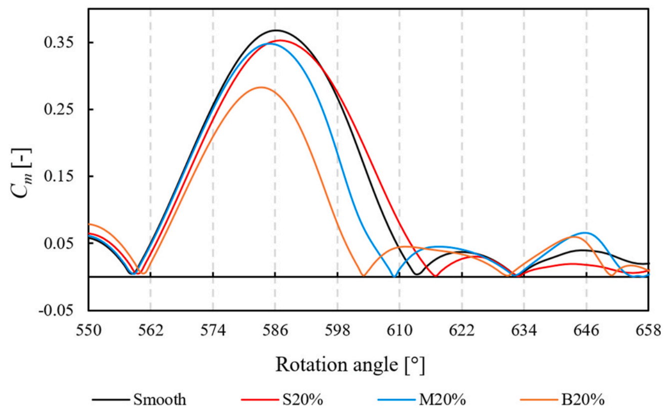

Fig. 10. Instantaneous turbine C_m under different surface roughness conditions.

3.4. Contours analysis

In order to understand the cause of performance reduction, this study analyzes the difference of some parameters at the surface of the blade. The reduced power coefficient is the result of the reduced moment being generated by the turbine. The CFD software calculates the moment acting on an object by integrating the pressure distribution across the object's surface. Therefore, it is crucial to examine the contours of pressure distribution across the surface of the turbine.

Fig. 11 shows the pressure distribution at the pressure side of the turbine blade. The right-most picture highlights the difference in $C_{pressure}$ between the smooth and fouled surface. It is shown that the fouled surface, especially near the leading edge, generates a lower pressure distribution than the smooth surface. Generally, the pressure side of the smooth surface has the same or higher pressure compared to the fouled surface.

Meanwhile, Fig. 12 depicts the turbine suction side's pressure distribution. It can be seen that the leading-edge pressure distribution on the fouled surface is also lower than the smooth surface. Opposite to Fig. 12, here the smooth surface has a slightly lower pressure than the fouled surface near the leading edge. Combining the pressure distribution between both sides of the turbine, the fouled surface yields a lower moment due to lower pressure differences. This result is in agreement with the previous study by Song et al. (2020).

To further clarify the influence of azimuthal blade position on the pressure distribution and its relation to torque generation, additional contour visualizations at an azimuth angle of 210° are presented below (Fig. 13). This position represents the downstream rotational region, where the blade experiences less favorable flow conditions and reduced pressure differences compared to the 90° azimuth position.

At the 210° azimuth position, the turbine blade experiences less favorable flow conditions due to stronger wake interaction during the downstream rotational phase. Under this condition, the pressure difference between the pressure and suction sides becomes weaker, particularly for the M20% roughness condition.

On the pressure side, the smooth blade maintains a more uniform high-pressure region near the leading edge, while the M20% condition

Table 7
Overview of C_p percentages for all roughness configurations relative to the smooth case.

Surface Conditions	*TSR* = 1.2		*TSR* = 1.6		*TSR* = 1.925		*TSR* = 2.29		*TSR* = 2.44		*TSR* = 2.8	
	C_p	Δ (%)	C_p	Δ (%)	C_p	Δ (%)	C_p	Δ (%)	C_p	Δ (%)	C_p	Δ (%)
Smooth	0.092	-	0.170	-	0.222	-	0.260	-	0.252	-	0.179	-
S10%	0.092	0%	0.169	1%	0.216	2%	0.254	2%	0.242	4%	0.174	3%
S20%	0.090	2%	0.163	4%	0.207	7%	0.241	7%	0.233	8%	0.168	6%
S40%	0.079	15%	0.140	17%	0.179	19%	0.207	20%	0.208	18%	0.152	15%
M10%	0.088	4%	0.156	8%	0.198	11%	0.231	11%	0.226	10%	0.164	8%
M20%	0.077	16%	0.137	19%	0.175	21%	0.201	23%	0.203	19%	0.149	17%
M40%	0.061	34%	0.105	38%	0.125	43%	0.131	50%	0.131	48%	0.093	48%
B10%	0.076	17%	0.135	20%	0.173	22%	0.198	24%	0.200	21%	0.147	18%
B20%	0.056	39%	0.094	45%	0.109	51%	0.108	58%	0.105	58%	0.068	62%

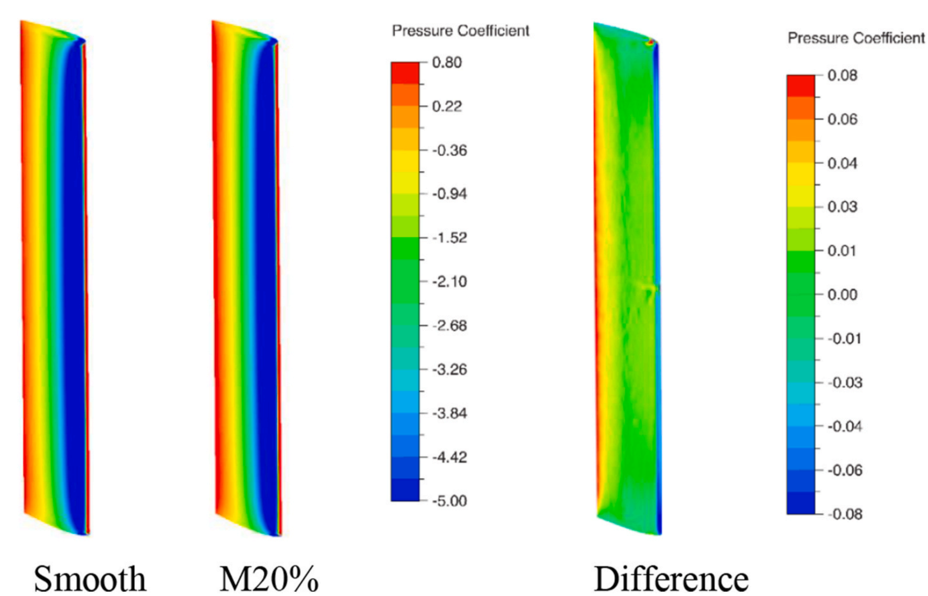

Fig. 11. Contours of $C_{pressure}$ distribution for the pressure side of the D-VAT at *TSR* 2.29 and azimuth angle of 90°.

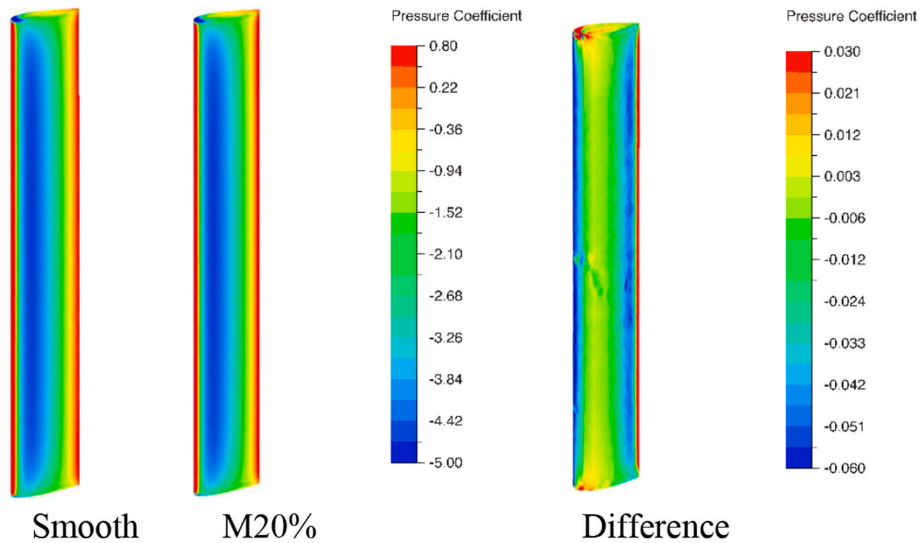

Fig. 12. Contours of $C_{pressure}$ distribution for the suction side of the D-VAT at *TSR* 2.29 and azimuth angle of 90°.

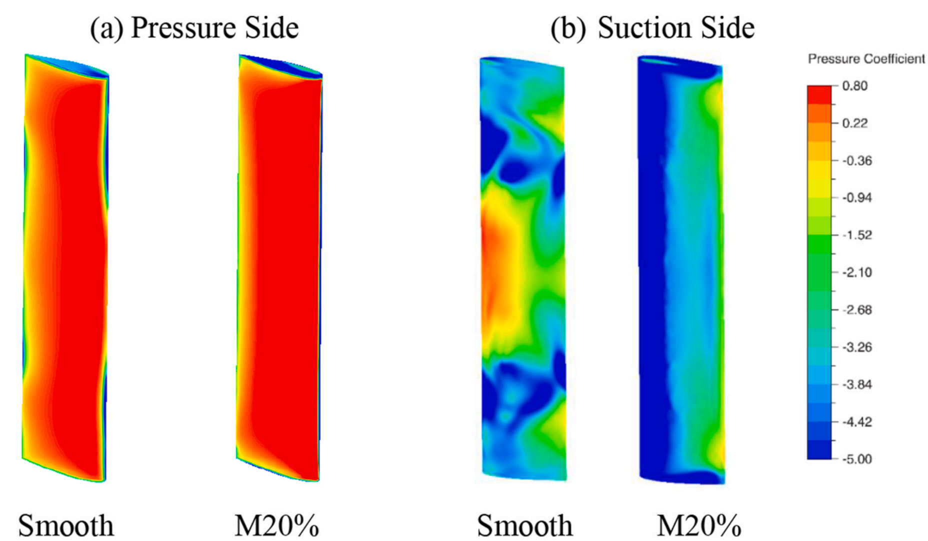

Fig. 13. Contours of $C_{pressure}$ distribution for the pressure side of the D-VAT at *TSR* 2.29 and azimuth angle of 210°.

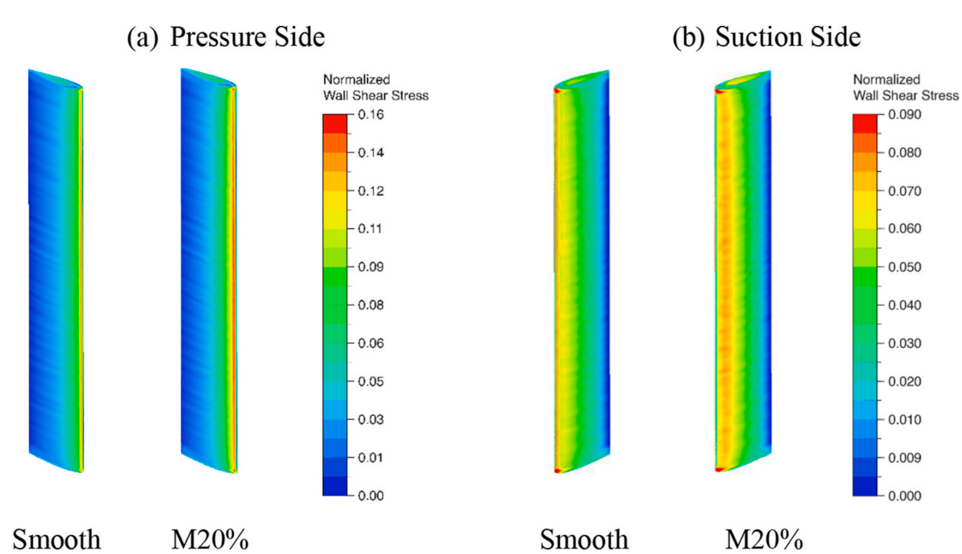

Fig. 14. Contours of wall shear stress distribution for the (a) pressure side and (b) suction of the D-VAT at *TSR* 2.29 and azimuth angle of 90°.

exhibits a less stable pressure distribution. More pronounced differences appear on the suction side, where the smooth blade still produces stronger low-pressure regions compared to the roughened blade. This indicates that surface roughness promotes earlier flow separation and weakens the suction effect around the blade surface. Consequently, the reduced pressure difference under the M20% condition contributes directly to lower instantaneous moment generation at the 210° azimuth position.

The weakening of the pressure difference observed in the previous analysis suggests that the surface roughness also modifies the near-wall flow behavior around the turbine blade. Therefore, further examination of the wall shear stress distribution is necessary to show the mechanism responsible for the pressure-field deterioration.

Observing the non-dimensional shear stress at the turbine surface further rectifies the cause of the turbine performance reduction. It is inferred that the fouled D-VAT tends to have a higher shear stress across its surface than the smooth D-VAT, as shown in Fig. 14(a) and (b). Fig. 14 shows that the fouled turbine generates a relatively higher value of shear stress (red contour) than the smooth turbine (green yellowish and blue contour) near the leading edge. This behavior further supports the previous pressure-field analysis, indicating that the increased near-wall shear stress induced by surface roughness contributes to stronger boundary-layer disturbance and promotes earlier flow separation around the blade surface.

Next analysis focuses on the Wall Shear Stress component along the Y-axis. An anomaly is evident under the B20% roughness condition, as depicted on the far right of Fig. 15, where all regions exhibit consistently low wall shear stress. This distribution is significantly different from the other roughness profiles, which exhibit more fluctuating contours. Such behavior suggests that large portions of the blade surface experience extensive flow separation under the B20% condition, reducing the effective momentum exchange near the wall and weakening the blade loading capability.

This phenomenon can be explained by observing the fluid response around the turbine blade. To analyze this, a cross-sectional view at the midpoint of the turbine blades, or 50% span, was taken. Fig. 15 represents the fluid flow around the turbine blade under specific conditions applied to all roughness profiles at a *TSR* of 2.29. The cross-sectional data in Fig. 16 were captured at the final time step of the simulation. The figure illustrates the progression of non-dimensional turbulent kinetic energy distribution within the rotary domain, starting from a smooth surface on the left and transitioning to increasingly rough surfaces toward the right.

The intensity of turbulent kinetic energy becomes particularly severe for the B20% roughness profile. This correlates with a 62% reduction in the *Cp*, as detailed in Table 7. These findings highlight the significant impact of surface roughness on turbine efficiency, particularly under severe conditions. Under these conditions, the turbine blade operates in a fully turbulent state, causing flow separation to occur across the entire blade surface. Consequently, the distribution of wall shear stress along the Y-axis in the B20% condition remains consistently low across all regions. This is attributed to the widespread flow separation throughout these areas. This condition significantly weakens the blade's ability to maintain effective pressure loading and stable torque generation during rotation. As a result, the severe roughness conditions lead to substantial turbine performance degradation, consistent with the large reduction in C_p observed in the previous analysis.

3.5. Mechanical power production and losses

Starting from the C_p value which is known and has been explained in Fig. 9, the mechanical power (P_{mech}) value can be calculated using equation (22). Although C_p is commonly used for performance comparison, the $_{Pmech}$ is also presented to provide a more intuitive interpretation of the turbine output in practical terms.

$$P_{mech} = 0.5\ .\ \rho\ .\ A\ .\ V^3\ .\ Cp \tag{22}$$

Parameter *A* represents the swept area, which in vertical turbines, this value can be expressed as the area of a rectangle (Width or Diameter x Height or Span) or defined as *D* is the turbine's diameter, which represents the parameter Width, and s is the turbine's span, representing the parameter Height, and ρ *of* 1025 kg/m^3 which is the density of seawater. From this equation, the mechanical power (P_{mech}) generated for each variation is shown in Fig. 17. The graph exhibits a trend similar to the C_p versus *TSR* in Fig. 9. This indicates that, for commercial operations, D-VATs must avoid surface roughness levels comparable to or worse than Medium or Big roughness. As shown in Fig. 17, these conditions result in a significant performance drop, leading to substantial losses on a commercial scale.

Further detailed comparisons of all surface roughness variations at two distinct *TSRs* reveal that the reduction in P_{mech} becomes more severe at higher *TSRs*. As illustrated in Fig. 18(a) and (b), the B20% variation causes a P_{mech} reduction of 39.28% under smooth surface conditions at a TSR of 1.2. This reduction becomes more worsens at a *TSR* of 2.8, increasing to 62%.These findings are also present in the previous study by Song et al. (2020). Although, the performance reduction at *TSR* of less than 3 is not as severe as in the present study. This may be attributed to the different turbine orientations. The experimental and numerical studies of Khanjanpour and Javadi (2020) also found that the power loss increases at a non-linear rate relative to the surface roughness increase.

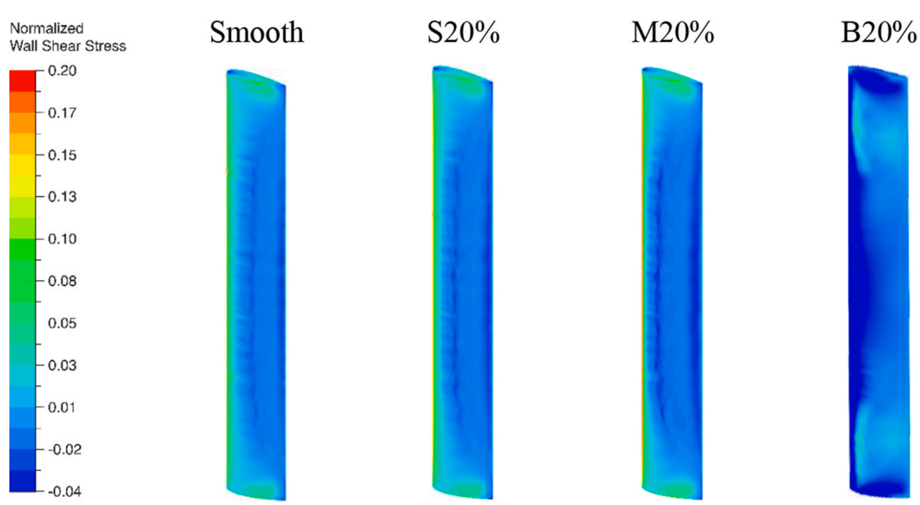

Fig. 15. Distribution of the wall shear stress component along the Y-axis on the D-VAT at *TSR* 2.29 and azimuth angle of 90°.

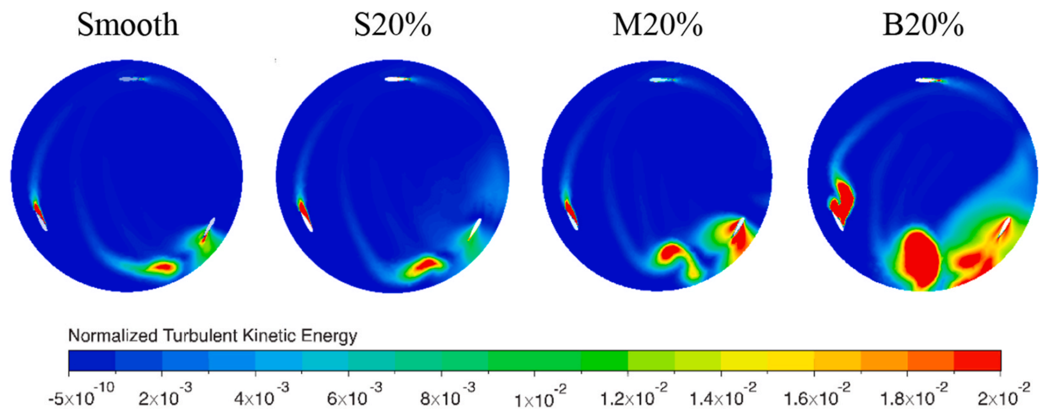

Fig. 16. Contours of normalized turbulent kinetic energy for the smooth and rough surface cases at *TSR* 2.29.

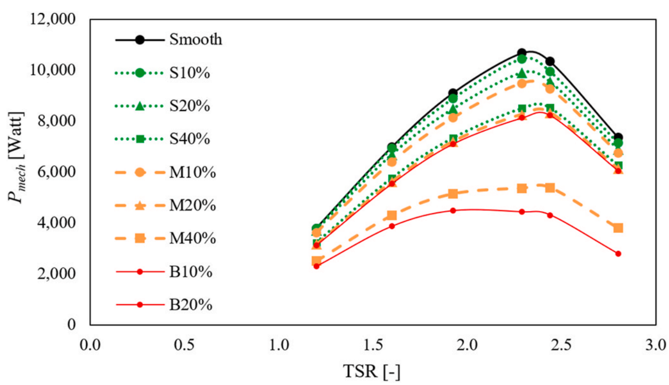

Fig. 17. P_{mech} response at different *TSR* for all roughness variations.

3.6. Operational performance degradation assessment

Marine biofouling on submerged turbine surfaces is a time-dependent phenomenon whose severity progressively increases during long-term operation in marine environments (Uzun et al., 2019). To address this, the present study introduces a simplified progressive roughness scenario to represent the gradual increase in surface degradation severity during prolonged exposure in tropical-equatorial waters.

The staged roughness progression adopted in this study was constructed based on the characteristic biofouling development trends reported by Uzun et al. (2019). for equatorial marine environments, where different fouling categories exhibit distinct characteristic development durations. In particular, slime-type fouling (Type C) develops rapidly during the early exposure period, followed by increasingly severe non-shell fouling (Type B) and calcareous fouling (Type A), which require longer exposure durations before reaching dominant growth conditions. Rather than reproducing exact biological growth behavior, the present approach uses these trends as representative operational stages for gradual roughness escalation. Accordingly, the eight roughness scenarios investigated in the present CFD study were grouped into representative long-term operational stages, as summarized in Table 8.

$$AEP = t_{op} \ . \ A_v \ . \ \mathrm{P_{mec}h} \tag{23}$$

In Eq. (23), t_{op} represents the operating duration assigned to each roughness condition based on the progressive roughness stages summarized in Table 8. Different t_{op} values were assigned to each stage to represent the gradual escalation of surface degradation severity during long-term marine exposure. The parameter A_v represents the annual device availability factor, which was adopted as 35% following the recommendation reported by (Paul, 2014). Meanwhile, the P_{mech} values were obtained from the simulations results presented in Table 7 using the representative operating condition at $TSR = 2.29$, which was selected to represent the nominal operational state of the turbine during long-term energy assessment.

Fig. 19 shows that the cumulative generated energy continues to increase throughout the operational period due to continuous turbine operation; however, the turbine efficiency progressively decreases as the representative roughness severity increases over time. During the initial clean condition, the turbine operates with a C_p of approximately 0.26, which gradually decreases to 0.254 and 0.241 under the S10% and S20% conditions, respectively. More significant degradation occurs during the intermediate and severe fouling stages, where the C_p further decreases to 0.207 under S40%, 0.201 under M20%, 0.131 under M40%, and finally reaches only 0.108 under the B20% condition.

The cumulative energy contribution from each operational stage also reflects this progressive degradation trend. During the mild roughness stages, the generated energy contribution corresponding to the assigned operational duration reaches approximately 96.01 kWh and 91.10 kWh for the S10% and S20% conditions, respectively. However, despite the longer operational duration assigned to the severe roughness stages, the generated energy decreases substantially due to the large reduction in turbine performance. The M40% condition produces only 63.27 kWh, while the B20% condition yields the lowest contribution of approximately 52.16 kWh. Relative to the smooth condition, the B20% scenario exhibits a reduction in C_p of approximately 58%. Although this degradation develops progressively throughout the operating period, its impact accumulates continuously and ultimately produces a substantial deficit in cumulative energy generation.

These results indicate that although cumulative energy generation naturally increases with operating time, the rate of energy accumulation becomes progressively lower as the turbine surface condition deteriorates. This trend becomes particularly noticeable after approximately 6000 operational hours, where the transition toward severe roughness conditions causes a sharp reduction in turbine efficiency, as shown by the significant drop in the C_p curve in Fig. 19. Beyond this operational period, the turbine experiences increasingly unfavorable energy conversion performance, where prolonged operation contributes relatively small additional energy gains compared to the severity of the associated efficiency degradation. While the reduction in C_p develops gradually throughout the operating period, its effect accumulates continuously, resulting in an increasingly pronounced gap in cumulative energy generation between the smooth and roughness-growth conditions. Consequently, prolonged operation without maintenance or surface cleaning may lead to substantial long-term energy production penalties in tropical marine environments.

4. Future studies

The present study is limited by the use of a URANS-based rough-wall-

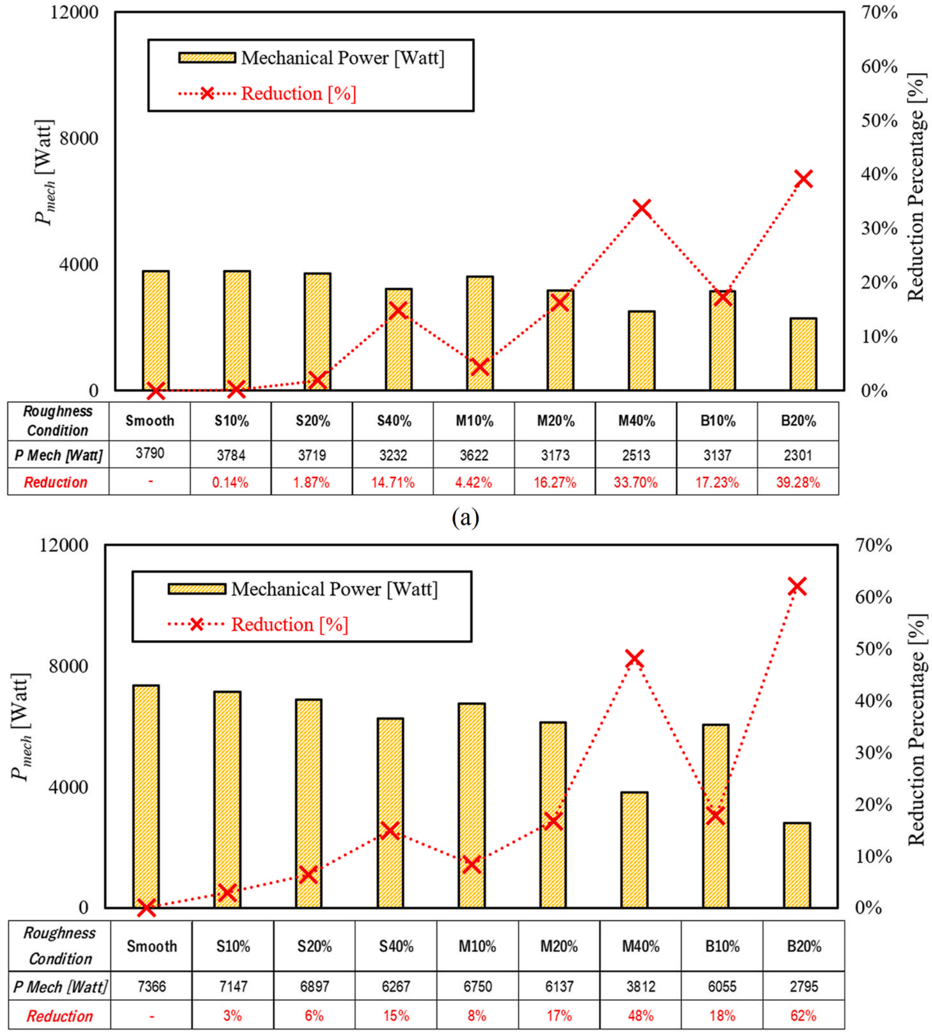

Fig. 18. P_{mech} reduction at (a) Low *TSR* and (b) High *TSR*.

Table 8
Representative progressive roughness stages adopted for the long-term operational assessment.

Operational Period	Dominant Fouling Severity	Representative Roughness Condition	Operating Hours
Day 0–10	Initial Clean Condition	Smooth	240 h
Day 10–100	Early mild fouling development	S10% and S20%	1080 h each
Day 100–250	Intermediate roughness progression	S40% and M20%	1800 h each
Day 250–365	Severe long-term fouling condition	M40% and B20%	1380 h each

function approach, where the surface roughness is represented virtually rather than through explicit biofouling geometry reconstruction. To further extend the present findings, future studies are recommended to investigate the D-VAT configuration using higher-fidelity approaches such as LES or DES, alongside explicit geometric roughness modeling and additional experimental validation under controlled marine or towing-tank conditions.

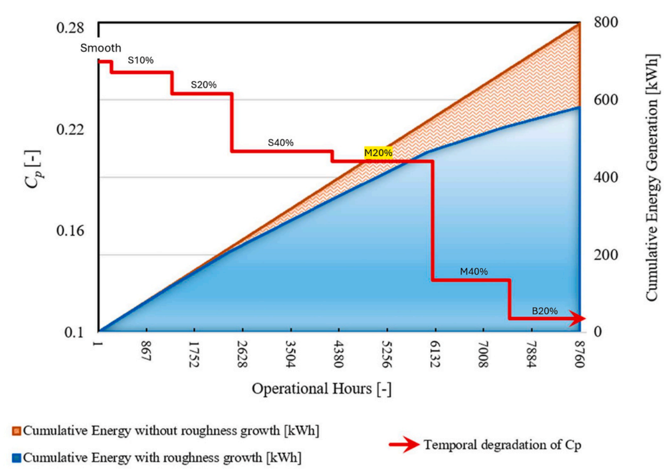

Fig. 19. Average annual energy production (AEP).

5. Conclusions

A 3D CFD simulation has been developed and validated to study the effect of surface roughness on the C_p of D-VAT. Eight roughness scenarios, varied by roughness height and surface coverage, are implemented in this study. This research demonstrates that decrease in C_p correlates linearly with the higher roughness height. This reduction in C_p has a direct impact on reducing power and energy production, as evidenced by the (S20%) configuration, which experienced a 2% decrease compared to a smooth surface at *TSR* 1.2. Furthermore, under the same *TSR* conditions, these decreases escalated to 39% in the (B20%) scenario. The most significant P_{mech} decrease happens with (B20%) scenario, amounting to a 62% decrease at a *TSR* of 2.8. A correlation was observed between *TSR* and P_{mech} under increasing surface roughness, where higher *TSR* conditions generally produced larger performance reductions. Therefore, operating at lower *TSR* conditions under severe roughness may help minimize performance penalties and maintain more stable power generation. A similar trend was observed in the cumulative energy generation analysis. Although cumulative energy output continues to increase over time, the rate of energy accumulation progressively decreases as roughness severity increases, particularly after approximately 6000 operational hours. Under severe roughness conditions such as B20%, significant reductions in C_p and instantaneous moment generation lead to substantially lower long-term energy production.These findings demonstrate that marine biofouling significantly affects both instantaneous turbine performance and long-term energy conversion capability. Therefore, periodic maintenance and surface-cleaning strategies are essential to maintain efficient turbine operation and minimize long-term energy losses in tropical marine environments.

CRediT authorship contribution statement

Dendy Satrio: Conceptualization, Data curation, Formal analysis, Funding acquisition, Investigation, Methodology, Supervision, Validation, Writing – original draft, Writing – review & editing. **Soonseok Song:** Conceptualization, Methodology, Supervision, Writing – review & editing. **Wakana Tsuru:** Formal analysis, Funding acquisition, Supervision, Writing – review & editing. **Mohammad Farid:** Data curation, Investigation, Software, Validation, Visualization, Writing – original draft. **Wimala Lalitya Dhanistha:** Formal analysis, Methodology, Writing – review & editing. **Maktum Muharja:** Formal analysis, Writing – review & editing. **Siti Musabikha:** Formal analysis, Writing – review & editing. **Herman Pratikno:** Formal analysis, Supervision, Writing – review & editing.

Declaration of competing interest

The authors declare that they have no known competing financial interests or personal relationships that could have appeared to influence the work reported in this paper.

Acknowledgments

The authors would like to convey their appreciation to the National Research and Innovation Agency (BRIN) for supporting the project under *Riset dan Inovasi untuk Indonesia Maju (RIIM) Kompetisi Gelombang IX* Program with contract number 3468/PKS/ITS/2025 and specifically 3853/PKS/ITS/2025. The authors also thank to the Institut Teknologi Sepuluh Nopember, which funded the relevant project under a scheme called Outbound Researcher Mobility (ORM) Program with contract number 2432/IT2/T/HK.00.01/2023. This study was also performed under the Joint Research Program at the Institute of Ocean Energy, Saga University under contract No. 25C06. We received the publication fee support from the Institute of Ocean Energy, Saga University, Japan.

References

Akhlagi, M., Farzad, G., Mehdi, M., Mohsen, S.R., 2023. Effective Parameters Optimization of a Small Scale Gorlov Wind Turbine , Using CFD Method 42.
Alkhabbaz, A., Hamza, H., Daabo, A.M., Yang, H.S., Yoon, M., Koprulu, A., Lee, Y.H., 2024. The aero-hydrodynamic interference impact on the NREL 5-MW floating wind turbine experiencing surge motion. Ocean Eng. 295, 116970. https://doi.org/10.1016/j.oceaneng.2024.116970.
ANSYS Inc, 2020. Ansys Fluent Theory Guide, 15317. ANSYS Inc., USA, pp. 724–746.
Celik, I.B., Ghia, U., Roache, P.J., Freitas, C.J., Coleman, H., Raad, P.E., 2008. Procedure for estimation and reporting of uncertainty due to discretization in CFD applications. J. Fluids Eng. Trans. ASME 130, 780011–780014. https://doi.org/10.1115/1.2960953.
Daabo, A.M., Alkhabbaz, A., Ibrahim, S.S., Hamzah, H., Hassan, A., Basem, A., Easa, H., Pavlovic, S., 2024. Thirteen vital factors for micro-scale radial turbine vane's design of geo-solar-powered Brayton cycle applications. Energy Convers. Manag. 315, 118774. https://doi.org/10.1016/j.enconman.2024.118774.
Darvehei, P., Bahri, P.A., Moheimani, N.R., 2018. Model development for the growth of microalgae: a review. Renew. Sustain. Energy Rev. 97, 233–258. https://doi.org/10.1016/j.rser.2018.08.027.
Demirel, Y.K., Uzun, D., Zhang, Y., Fang, H.C., Day, A.H., Turan, O., 2017. Effect of barnacle fouling on ship resistance and powering. Biofouling 33, 819–834. https://doi.org/10.1080/08927014.2017.1373279.
Erwandi, E., Kasharjanto, A., Satrio, D., Rahuna, D., Suyanto, E.M., Mintarso, C.S.J., Irawanto, Z., Ramadhani, M.A., 2024. Numerical analysis of resistance and motions on trimaran floating platform for tidal current power plant. Int. Rev. Model. Simulations 17, 6–16. https://doi.org/10.15866/iremos.v17i1.24366.
Etemadeasl, V., Esmaelnajad, R., Gharlai, K., Riasi, A., 2025. Application of entropy production theory for evaluating the performance of a gorlov hydrokinetic turbine. Iran. J. Sci. Technol. Trans. Mech. Eng. 49, 669–688. https://doi.org/10.1007/s40997-024-00803-9.
Farkas, A., Degiuli, N., Martić, I., Barbarić, M., Guzović, Z., 2022. The impact of biofilm on marine current turbine performance. Renew. Energy 190, 584–595. https://doi.org/10.1016/j.renene.2022.03.134.
Ffield, A., Robertson, R., 2008. Temperature finestructure in the Indonesian seas. J. Geophys. Res. Oceans 113, 1–19. https://doi.org/10.1029/2006JC003864.
Firdaus, A., Houlsby, G., Adcock, T., 2017. Opportunities for tidal stream energy in Indonesian waters. In: Proceedings of the Twelfth European Wave and Tidal Energy Conference, pp. 887.1–887.7.
Ghafoorian, F., Reza, S., Wan, H., 2024. Numerical study on aerodynamic performance improvement and efficiency enhancement of the savonius vertical axis wind turbine with semi-directional airfoil guide vane. Ocean Eng. 307, 118186. https://doi.org/10.1016/j.oceaneng.2024.118186.
Grigson, C., 1992. Drag losses of new ships caused by hull finish. J. Ship Res. 36, 182–192.
Hadiyanto, 2018. Fouling polychaetes in tanjung priok port of Jakarta, Indonesia. ASEAN J. Sci. Technol. Dev. 35, 79–87.
Hasfanizam, M., Yazik, M., Hafiz, M., Najah, A., 2024. One-way fluid structure interaction analysis of a static savonius hydrokinetic turbine under different velocity and surface roughness with different blade materials. Ocean Eng. 291, 116373. https://doi.org/10.1016/j.oceaneng.2023.116373.
Khanjanpour, M.H., Javadi, A.A., 2020. Experimental and CFD analysis of impact of surface roughness on hydrodynamic performance of a Darrieus Hydro (DH) turbine. Energies 13. https://doi.org/10.3390/en13040928.
Kusuma, D.W., Murdimanto, A., Aden, L.Y., Sukresno, B., Jatisworo, D., Hanintyo, R., 2017. Sea surface temperature dynamics in Indonesia. IOP Conf. Ser. Earth Environ. Sci. 98. https://doi.org/10.1088/1755-1315/98/1/012038.
Madi, M., Mukhtasor, M., Rahmawati, S., Satrio, D., Tuswan, T., Ismail, A., 2024. Experimental study on the effect of single flow disturber on the performance of the straight-bladed hydrokinetic turbine at low current speed. Pomorstov 38, 43–54. https://doi.org/10.31217/p.38.1.4.
Mannion, B., Leen, S.B., Nash, S., 2018. A two and three-dimensional CFD investigation into performance prediction and wake characterisation of a vertical axis turbine. J. Renew. Sustain. Energy 10. https://doi.org/10.1063/1.5017827.
Moroso, A., 2007. The Italian Ship Model Basin the Kobold Marine Turbine: from the Testing Model to the Full Scale Prototype.
Ouro, P., Stoesser, T., 2019. Impact of Environmental Turbulence on the Performance and Loadings of a Tidal Stream Turbine, pp. 613–639.
Pattanapol, W., Wakes, S.J., Hilton, M.J., Dickinson, K.J.M., 2008. Modeling of surface roughness for flow over a complex vegetated surface. Int. J. Eng. Nat. Sci. 2, 18–26.
Paul, L., 2014. Electricity Form Wave and Tide. John Wiley & Sons Ltd.
Porté-agel, F., Bastankhah, M., Shamsoddin, S., 2020. Wind-Turbine and Wind-Farm Flows : a Review, Boundary-Layer Meteorology. Springer, Netherlands. https://doi.org/10.1007/s10546-019-00473-0.
Priegue, L., Stoesser, T., 2017. The influence of blade roughness on the performance of a vertical axis tidal turbine. Int. J. Mar. Energy 17, 136–146. https://doi.org/10.1016/j.ijome.2017.01.009.
Rezaeiha, A., Montazeri, H., Blocken, B., 2018. Towards accurate CFD simulations of vertical axis wind turbines at different tip speed ratios and solidities: guidelines for azimuthal increment, domain size and convergence. Energy Convers. Manag. 156, 301–316. https://doi.org/10.1016/j.enconman.2017.11.026.
Richardson, L.F., 1910. The approximate arithmetical solution by finite differences of physical problems involving differential equations, with an appliccation to the stresses in a masonry dam. Phys. Trans. R. Soc. A 210, 307–357.
Robinson, D.F., Hassan, H.A., 1996. A two-equation turbulence closure model for wall bounded and free shear flows. Fluid Dyn. Conf. 1–11. https://doi.org/10.2514/6.1996-2057, 1996.
Satrio, D., Adipradana, R.A., Mubarok, M.A., Muharja, M., Tuswan, Hakim, M.L., Ridhwan, N.A., Madi, Ismail, A., Musabikha, S., 2026. Enhanced performance of cross-flow savonius turbines at low current velocity : a numerical investigation on the influence of deflector. Nase More 73. https://doi.org/10.17818/NM/2026/1.2.

Satrio, D., Erwandi, Rahuna, D., 2025. Investigation of enhanced peak lift performance and stall angle delay by attachment of Vortex generators on blade surfaces of vertical axis ocean current turbine. Ocean Eng. 326, 120762. https://doi.org/10.1016/j.oceaneng.2025.120762.

Satrio, D., Suntoyo, Widyawan, H.B., Ramadhani, M.A., Muharja, M., 2024. Effects of the distance ratio of circular flow disturbance on vertical-axis turbine performance: an experimental and numerical study. Sustain. Energy Technol. Assessments 63, 103635. https://doi.org/10.1016/j.seta.2024.103635.

Shi, W., Wang, Dazheng, Atlar, M., Wang, Dan, 2013. Similarity laws and model test approaches to determine hydrodynamic performance of A marine. Turbine 697, 665–672. https://doi.org/10.4028/www.scientific.net/AMR.694-697.665.

Song, S., Demirel, Y.K., Atlar, M., Shi, W., 2020. Prediction of the fouling penalty on the tidal turbine performance and development of its mitigation measures. Appl. Energy 276, 115498. https://doi.org/10.1016/j.apenergy.2020.115498.

Starzmann, R., Kaufmann, N., Jeffcoate, P., Guerra, M., Hay, A., Pieroway, R., 2022. Effect of fouling on the performance of an instream turbine. Int. Mar. Energy J. 5, 229–237. https://doi.org/10.36688/imej.5.229-237.

Tayman, J., Swanson, D.A., 1999. On the validity of MAPE as a measure of population forecast accuracy. Popul. Res. Pol. Rev. 18, 299–322. https://doi.org/10.1023/A:1006166418051.

Tuncer, C., Peter, B., 1984. Physical an Computational Aspect of Convective Heat Tranfer.

Utama, I.K.A.P., Satrio, D., Mukhtasor, M., Atlar, M., Shi, W., Hantoro, R., Thomas, G., 2020. Numerical simulation of foil with leading-edge tubercle for vertical-axis tidal-current turbine. J. Mech. Eng. Sci. 14, 6982–6992. https://doi.org/10.15282/jmes.14.3.2020.02.0547.

Uzun, D., Demirel, Y.K., Coraddu, A., Turan, O., 2019. Time-dependent biofouling growth model for predicting the effects of biofouling on ship resistance and powering. Ocean Eng. 191, 106432. https://doi.org/10.1016/j.oceaneng.2019.106432.

Walker, J.S., Green, R.B., Gillies, E.A., Phillips, C., 2020. The effect of a barnacle-shaped excrescence on the hydrodynamic performance of a tidal turbine blade section. Ocean Eng. 217, 107849. https://doi.org/10.1016/j.oceaneng.2020.107849.

Yassin, K., Kassem, H., Stoevesandt, B., Klemme, T., Peinke, J., 2021. Numerical Investigation of Aerodynamic Performance of Wind Turbine Airfoils with Ice Accretion, pp. 1–20.

Zhao, G., Yang, R.S., Liu, Y., Zhao, P.F., 2013. Hydrodynamic performance of a vertical-axis tidal-current turbine with different preset angles of attack. J. Hydrodyn. 25, 280–287. https://doi.org/10.1016/S1001-6058(13)60364-9.